

## CHARACTERIZATION OF THE SECONDARY FLOW IN TURBULENT RECTANGULAR DUCTS WITH VARYING ASPECT RATIO

**Ricardo Vinuesa**

Linné FLOW Centre, KTH Mechanics  
SE-100 44 Stockholm, Sweden  
rvinuesa@mech.kth.se

**Philipp Schlatter**

Linné FLOW Centre, KTH Mechanics  
SE-100 44 Stockholm, Sweden  
pschlatt@mech.kth.se

**Hassan M. Nagib**

MMAE Department, Illinois Institute of Technology  
Chicago, IL 60616, USA  
nagib@iit.edu

### ABSTRACT

Direct numerical simulations of turbulent duct flows with width-to-height ratios 1, 3, 5, 7 and 10, at a friction Reynolds number  $Re_{\tau,c} \simeq 180$ , are carried out with the spectral element code Nek5000. The aim of these simulations is to gain insight into the kinematics and dynamics of Prandtl's secondary flow of second kind, and its impact on the flow physics of wall-bounded turbulence. The secondary flow is characterized in terms of the cross-plane mean kinetic energy  $K = (V^2 + W^2)/2$ , and its variation in the spanwise direction of the flow. Our results show that averaging times of at least 3,000 time units are required to reach a converged state of the secondary flow, which extends up to  $z^* \simeq 5h$  from the side walls. We also show that if the duct is not wide enough to accommodate the whole extent of the secondary flow, then its structure is modified by means of a different spanwise distribution of energy. The kinetic energy of the secondary flow for  $z^* > 5h$  in aspect ratios 7 and 10 exhibits a decaying level of energy, and the rate of decay is approximately  $\langle K_{yz} \rangle \sim T_A^{-1}$ . This is the same rate of decay observed in a spanwise-periodic simulation, which suggests that at the core,  $\langle K \rangle_{yz}$  behaves as a random variable with zero mean, with rate of decay consistent with central limit theorem theory. Non-stationary effects of the secondary flow may persist into the core for all the aspect ratios we have run so far, and may interact with the dynamics of the nominally homogeneous flow that would exist in a channel. The non-stationary effects will be presented and further discussed in the Symposium. Note that these conclusions are limited to the low Reynolds number range under consideration, and additional data will be necessary to assess Reynolds number effects.

### INTRODUCTION

Turbulent duct flows of different aspect ratios AR (defined as the duct width  $W$  divided by its total height  $H$ ) are of great importance for a number of technological applications. The most remarkable characteristic of ducts is the formation of the so-called Prandtl's secondary flow of second kind at the duct corners, which arises from the Reynolds stress difference  $\overline{v^2} - \overline{w^2}$  and the deviatoric Reynolds shear

stress  $\overline{vw}$ . Due to the Reynolds-stress-induced nature of this kind of secondary flow, currently available Reynolds Averaged Navier–Stokes (RANS) models widely used in industry in general fail to predict its effect on the flow. The studies by Gavrilakis (1992), Huser & Biringen (1993), Uhlmann *et al.* (2007) and Pinelli *et al.* (2010) have shown the potential of using numerical simulations to study turbulent duct flows. They performed direct numerical simulations (DNSs) of square ducts at low Reynolds numbers below  $Re_{\tau} = 300$ . The velocity and length scales are the friction velocity  $u_{\tau} = \sqrt{\tau_w/\rho}$  (where  $\tau_w$  is the mean shear stress at the wall and  $\rho$  is the fluid density) and the duct half-height  $h$  respectively, whereas  $Re_{\tau}$  is the friction Reynolds number. On the other hand, the impact of the secondary flow on the mean velocity profile and the turbulent fluctuations for increasing aspect ratios has not been characterized in detail before, and this is the aim of the present study.

### NUMERICAL SIMULATIONS

Turbulent duct flows with aspect ratios 1, 3, 5, 7 and 10 at  $Re_{\tau,c} \simeq 180$  (where  $u_{\tau,c}$  is the friction velocity at the duct centerplane in the spanwise direction) are simulated by means of DNS. The database was initially presented by Vinuesa *et al.* (2014b, 2015c). The simulations were performed with the code Nek5000, developed by Fischer *et al.* (2008) and based on the spectral element method (SEM) by Patera (1984). In the SEM the computational domain is decomposed into elements, and the solution is expanded in terms of Legendre polynomials of order  $N$  inside those elements. The location of the nodes within elements is fixed, and follows the Guass–Lobatto–Legendre (GLL) distribution, whereas there are no restrictions regarding the position of the elements in the domain. This means that this method allows the flexibility to compute complex geometries, while still preserving the characteristics of a high-order spectral method. In the present study we considered the  $\mathbb{P}_N - \mathbb{P}_{N-2}$  formulation with  $N = 11$ . Therefore, the velocity field was expanded in terms of Legendre polynomials of order 11, and order 9 was considered for the pressure field. The nonlinear terms are treated explicitly by third-order extrapolation (EXT3), whereas the viscous

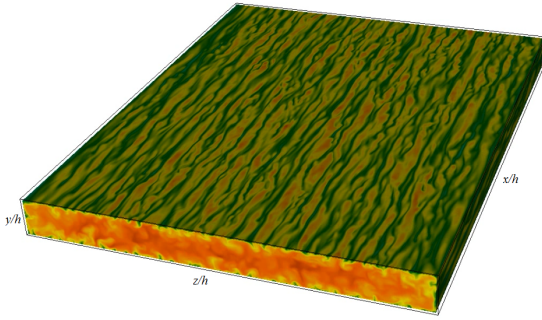


Figure 1. Instantaneous streamwise velocity from the aspect ratio 10 case at 2,000 convective time units from the beginning of the simulation. Green and orange represent minimum and maximum velocities in the field respectively. Flow is from lower left to upper right, and walls have been removed for clarity.

terms are treated implicitly by a third-order backward differentiation scheme (BDF3). Nek5000 is written in Fortran 77 and C, and parallelized with MPI. Parallel I/O is supported both through MPI I/O and a custom parallel I/O implementation. Over 190 users worldwide employ Nek5000 for their research and it has been acknowledged in more than 200 journal articles. Besides the duct cases, we have used Nek5000 to compute the flow around a wing section represented by a NACA4412 profile (Vinuesa *et al.*, 2015a) and around a wall-mounted square cylinder (Vinuesa *et al.*, 2015b). During the runs we compute a total of 71 statistical fields where streamwise-homogeneity is exploited, which allow us to calculate complete turbulence budgets. For flow visualizations we use the open source massively parallel visualization tool VisIt (<https://visit.llnl.gov/>).

With respect to the flow setup, periodicity is assumed in the streamwise direction  $x$  in all the cases, and no-slip conditions are imposed at the walls along the vertical ( $y$ ) and spanwise ( $z$ ) directions. All the ducts have a streamwise length of  $L_x = 25h$ , and the same Reynolds number  $Re_{b,c} \simeq 2,800$  is maintained in the centerplane for all the aspect ratio cases ( $Re_{b,c}$  is based on centerplane bulk velocity and  $h$ ). All the simulations are started from a laminar solution, and transition to turbulence is tripped by means of a localized volume force acting in  $y$ . Its parameters are designed to create strong, stationary streaks that lead to rapid turbulent breakdown as described by Schlatter & Örlü (2012). Figure 1 shows an instantaneous streamwise velocity field obtained from the duct with  $AR = 10$ . Near-wall streaks can be easily identified in this figure, with the well documented spacing in the spanwise direction  $\Delta z^+ \simeq 100$ . The resolution is therefore appropriate to capture near-wall dynamics in the flow, and the use of a high-order method improves the representation of the velocity field. It is interesting to observe how near-wall streaks are also formed on the side walls, also with an approximate spacing of  $\Delta y^+ \simeq 100$ , and how at the corner the effect of the two walls inhibits the formation of such structures. Instead, the flow field in Figure 1 shows how the bursting events from horizontal and vertical walls interact at the corner. These interactions were reported by Huser & Biringen (1993) to result in a redistribution of energy from  $v^2$  to  $w^2$  in square ducts, which eventually leads to the formation of the mean secondary flow.

Regarding the role of coherent structures in the ducts from a dynamical point of view, we considered several widely used methods for coherent structure identification, including  $\lambda_2$  (Jeong & Hussain, 1995),  $Q$  (Hunt *et al.*, 1998),  $\lambda_{ci}$  (Zhou & Kendali, 1999) and  $\Delta$  (Chong *et al.*, 1990), together with a less widely used approach by Kida & Miura (1998), from a number of instantaneous realizations of the flow (Nagib *et al.*, 2014). The main difference between the latter and the other methods is the fact that it is based on explicitly seeking pressure minima, and is defined on two-dimensional planes of the fields (unlike the other techniques which are defined in three-dimensional realizations). All the methods produce very similar results, and identify the occurrence of buffer layer vortices along the horizontal and side walls, exhibiting the spacing between streaks of  $\simeq 100^+$  observed in Figure 1. Coherent vortex analyses show two interesting results: the first one is that, unlike in the spanwise periodic channel, in the duct the number of streaks present in the flow is limited by the width scaled in wall units. The second conclusion is that no coherent structures are detected close to the corners (as also observed in Figure 1), which could be explained by the fact that the two walls inhibit the regular near-wall cycle of turbulence and therefore condition the presence of coherent vortices in this region. In addition to this, our results indicate that coherent vortices statistically exhibit essentially the same length in the streamwise direction in duct flows of aspect ratios from 1 to 10 and in spanwise-periodic channel flows. This means that from a dynamical perspective, rectangular ducts and channels exhibit similar features, although due to the different boundary conditions at the side walls the kinematic behavior of the flows differ, as will be discussed next.

## CHARACTERIZATION OF THE SECONDARY FLOW

The secondary flow in rectangular ducts is evaluated by analyzing the two-dimensional fields obtained after averaging over the two statistically homogeneous dimensions of the flow: streamwise and time. It is in these averaged fields where the secondary flow is observed, as shown in Figure 2 for the aspect ratio 1 and 3 cases. As shown in this figure, the secondary flow lies on the  $yz$  plane, and consists of eight counter-rotating vortices located close to the side walls, which convect momentum towards the corners. Whereas in the square duct case all the vortices exhibit the same size and momentum is convected towards the corner bisector, Figure 2 shows that in rectangular ducts the vortex located on the horizontal wall is wider in the spanwise direction, and the one on the side wall is slightly smaller than the corresponding one in the square case. It is important to note that these vortices are a mean flow feature, and therefore are only observed in time-averaged fields, not in instantaneous representations of the flow. In other words, they do not play an obvious role in the instantaneous dynamics of the duct, and it is the kinematic response of the flow, with the need to satisfy the no-slip conditions at the side walls, what produces them. In spanwise-periodic channel flows these boundary conditions at the side walls do not have to be satisfied, and therefore the mean velocity components  $V$  and  $W$  eventually decay to zero everywhere when statistical convergence is reached.

In the present study we characterize the secondary flow in terms of its kinetic energy  $K = (V^2 + W^2)/2$  at various

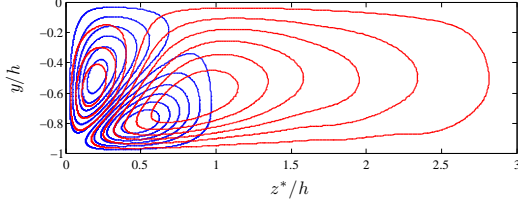


Figure 2. Streamlines showing the secondary flow corresponding to the (blue) square and (red) aspect ratio 3 duct cases (note that  $z^*$  is measured from the corner to allow easier comparison between the two cases.). Flow field obtained after streamwise- and time-averaging.

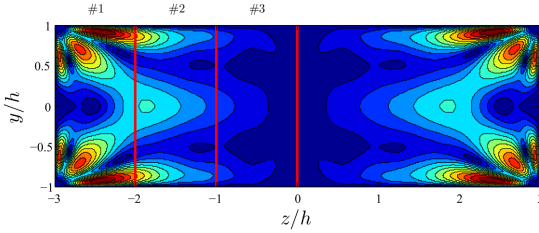


Figure 3. Kinetic energy of the secondary flow  $K$  for the AR = 3 case, and windows used to calculate  $\langle K \rangle_{yz}$ .

locations in the spanwise direction  $z$ . To do that, we divide the rectangular ducts into smaller areas of width  $h$  and height  $2h$ . Consequently, the square duct would be divided into two regions, and the AR = 10 case into 20. The symmetry of the flow with respect to the  $z/h = 0$  plane can be exploited to improve the statistics, which leads to a total of 10 areas in the AR = 10 case. This is illustrated for the AR = 3 and 10 cases in Figures 3 and 4, where contour maps of  $K$  are also shown. Note that  $K$  shows the secondary flow distribution with the counter-rotating vortices, and the spanwise extent of the cross-flow. It is interesting to observe that in the AR = 3 case the secondary flow extends up to a spanwise length of  $z^* \simeq 3h$  (where  $z^*$  is measured starting from the corner), whereas the wider AR = 10 duct allows the cross-flow to develop up to  $z^* \simeq 5h$ . With respect to the windows, as a convention we will denote the one closest to the corner as #1, and increase the number up to the value of the one closer to the core of the duct. As shown in Figure 4, in the aspect ratio 10 case the window from  $z = -10h$  to  $-9h$  would be #1, and the one from  $z = -h$  to 0 would be #10. The idea is to track the evolution in time of the secondary flow kinetic energy  $K$  averaged over these windows, to assess both their respective rates of convergence and their converged values. We will use the symbol  $\langle \cdot \rangle$  to denote the spatial average of a certain quantity, whereas capital letters denote the mean in time (so  $V$  would be the time-average of the instantaneous signal  $\bar{v}$ ). Here we will consider the value of  $K$  averaged in the vertical direction, and also in the spanwise direction in a particular window.

The results from the previous procedure applied to the first window, denoted by  $\langle K \rangle_{yz1}$ , are shown in Figure 5. The value of the secondary flow kinetic energy averaged over the first window (which is the only one present in the square duct) is represented as a function of the averaging

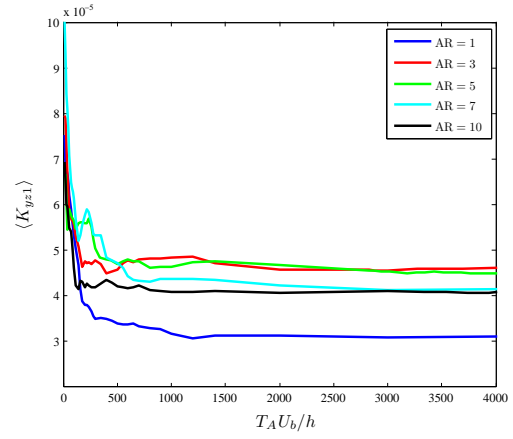


Figure 5. Kinetic energy of the secondary flow averaged over the first window  $\langle K_{yz1} \rangle$  as a function of averaging time, for all the aspect ratios.

time  $T_A U_b/h$  (note that the reported averaging periods exclude the initial transients). All the aspect ratio cases reach a fully converged state after approximately 3,000 convective time units, and the square duct shows the lowest level of energy:  $\langle K_{yz1} \rangle \simeq 3 \times 10^{-5}$ . Aspect ratios 3 and 5 exhibit values of around  $4.5 \times 10^{-5}$ , whereas the highest aspect ratios 7 and 10 have a slightly lower  $\langle K_{yz1} \rangle$  value of  $4 \times 10^{-5}$ . As we will discuss below, these differences have to do with the spanwise development of the secondary flow: the square duct does not allow the cross-flow to evolve and reach the form it would exhibit in a sufficiently wider duct. With respect to aspect ratios 3 and 5, they show a pattern closer to the wider 7 and 10 cases, but constrained on a narrower space, which leads to higher concentration of energy close to the corner.

Figure 6 shows the kinetic energy of the secondary flow averaged over the second and third windows (excluding the square duct), as a function of averaging time. The second window from all the cases exhibit a very similar converged level of energy (after averaging for at least 3,000 time units) of  $\langle K_{yz2} \rangle \simeq 2 \times 10^{-5}$ , which suggests that beyond a certain width the secondary flow, initiated at the corner, shares common features in all the ducts. Comparison of the second windows from aspect ratios 3 and 10 in Figures 3 and 4 supports this observation. Interestingly, the third window from aspect ratios 5, 7 and 10 show a very similar level of energy  $\langle K_{yz3} \rangle \simeq 5 \times 10^{-6}$ , whereas the energy corresponding to the AR = 3 case is lower:  $2.5 \times 10^{-6}$ . If we again compare the third windows from Figures 3 and 4 it becomes obvious that the secondary flow from the aspect ratio 10 case is still developing in  $z^*$ , and since this is the last window of the AR = 3 case the cross-flow cannot evolve further, producing a lower level of energy.

The core of the duct is characterized for the aspect ratios 7 and 10 in Figure 7. In this figure we show the values of  $\langle K_{yz} \rangle$  integrated over windows #6 and #7 in the AR = 7 case, and windows #6, #7 and #10 in the AR = 10 duct, as a function of averaging time. We also show the results of a channel flow simulation (where spanwise periodicity was imposed), performed with the Fourier–Chebyshev spectral code SIMSON (Chevalier *et al.*, 2007), in a computational domain with same streamwise length as the duct cases ( $L_x = 25h$ ) and with a ratio between spanwise and

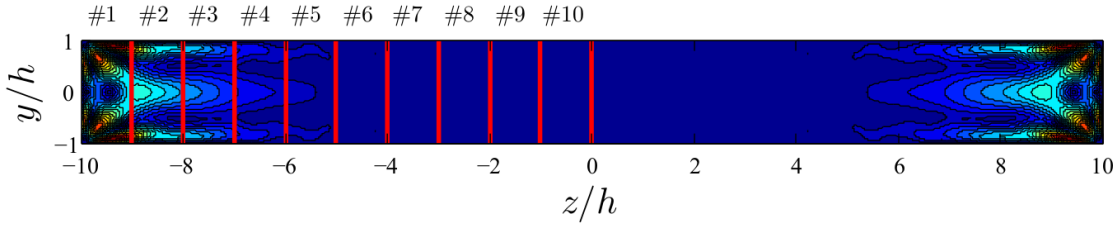


Figure 4. Kinetic energy of the secondary flow  $K$  for the AR = 10 case, and windows used to calculate  $\langle K \rangle_{yz}$ .

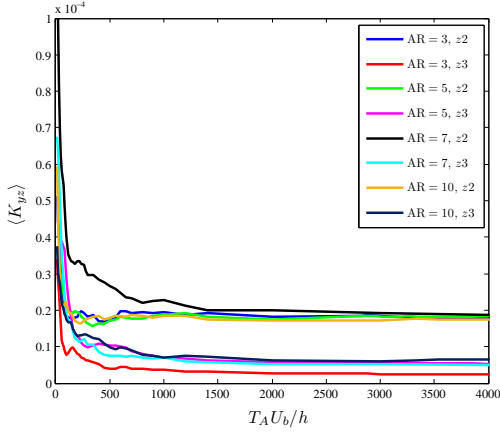


Figure 6. Kinetic energy of the secondary flow averaged over the second and third windows as a function of averaging time, for aspect ratios 3, 5, 7 and 10.

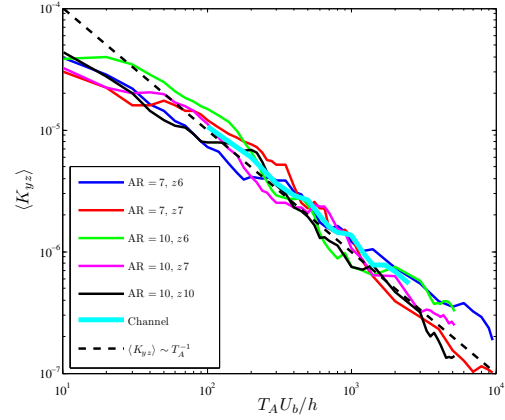


Figure 7. Kinetic energy of the secondary flow averaged over windows #6 and #7 in the AR = 7 case, and over windows #6, #7 and #10 in the AR = 10 configuration. This quantity is shown as a function of averaging time. The same variable is shown averaged over the cross-sectional area in a spanwise-periodic channel, together with the observed rate of decay  $\langle K_{yz} \rangle \sim T_A^{-1}$ .

wall-normal lengths  $L_z/L_y = 5$ . For the channel results we considered a single window spanning the whole width of the periodic domain, although the same trend is obtained by assuming windows of different sizes. Note that these windows were chosen due to the fact that, as observed in Figure 4, the long-time average of the secondary flow exhibits a spanwise length of about  $z^* \simeq 5h$ , and we are interested in comparing the energy of the vortices at the core of the duct and the ones in the channel. Interestingly, the value of  $\langle K_{yz} \rangle$  decays as the averaging time increases in all the windows and in the channel, and both flows exhibit the same rate of decay  $\langle K_{yz} \rangle \sim T_A^{-1}$ . This suggests that, at the core, the kinetic energy of the secondary flow is in fact a random variable with zero mean. Thus, increasing the averaging time (or the number of samples in statistics terms) leads to progressively lower values. This also implies that the rate of convergence of the cross-plane velocities  $V$  and  $W$  would be  $\sim T_A^{-1/2}$ . This is consistent with theory based on central limit theorem, and our results indicate that this value is independent of AR. Besides, similar values of  $K$  are obtained for comparable averaging times. Consequently, the long-time average of the kinematics found in a spanwise-periodic channel and at the core of a wide enough duct are similar, and Figure 7 is a manifestation of sufficiently converged statistics.

The fourth and fifth windows are analyzed for aspect ratios 5, 7 and 10 in Figure 8. It is interesting to note that although the levels of energy from the various cases do not decay at the rate  $\langle K_{yz} \rangle \sim T_A^{-1}$ , it is not clear whether the data would converge to a nonzero value or not. In any case, the behavior in this region is different from the one observed at the core, where the rate of decay is consistent with the

one exhibited by a spanwise-periodic channel, and therefore it can be stated that in windows #4 and #5 the flow does not behave as it does in the channel. The fourth window exhibits the same trend in AR = 7 and 10, with higher energy level than the corresponding window in the AR = 5 duct. This is same behavior (with lower energy levels) is observed in window #5, which further confirms the similarities of ducts with AR  $\geq 7$ , and the constrained secondary flow in narrower ducts.

After assessing the levels of energy associated with the secondary flow at localized regions in the duct, we evaluate the spanwise variation of the kinetic energy integrated in the wall-normal direction  $\langle K_y \rangle$ . Figure 9 shows this quantity for all the ducts under consideration in this study, as a function of the spanwise coordinate  $z^*$ , which is measured from the corner. This figure shows that the secondary flow is stronger close to the corner, and becomes gradually attenuated as the core of the duct is approached. It is also interesting to note that although all the aspect ratios show a similar structure, with two local maxima and one local minimum in between, their actual values are strongly influenced by the constraining effect of the aspect ratio. Thus, AR determines the structure of the secondary flow, where for instance it is clear that the square duct exhibits a higher concentration of energy close to the corner and has a steeper decay of kinetic energy as the centerplane is approached. This is also consistent with Figure 5, where we show that the integrated value of  $K$

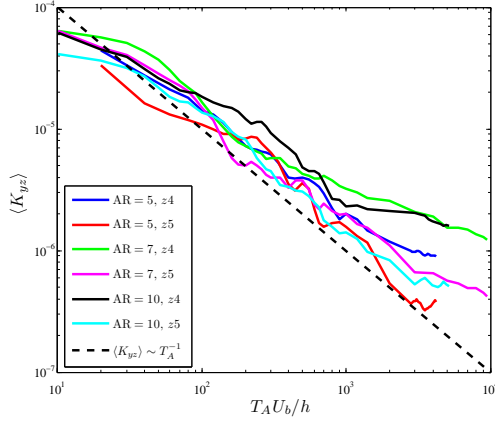


Figure 8. Kinetic energy of the secondary flow averaged over the fourth and fifth windows as a function of averaging time, for aspect ratios 5, 7 and 10. Rate of decay  $\langle K_{yz} \rangle \sim T_A^{-1}$  shown for comparison purposes.

over that first window is lower in the square duct, and provides additional support to the claim that the duct develops similar features in all the aspect ratios if the width is large enough. The significantly larger maximum of  $\langle K_y \rangle$  close to the corner in the square duct (between 30% and 44% larger than the other cases) is also remarkable. It is also interesting to observe that the aspect ratio 7 and 10 cases exhibit a similar peak value of  $\langle K_y \rangle$  close to the corner, whereas AR = 3 and 5 show intermediate values, highlighting the developing nature of the secondary flow with AR. The ducts with aspect ratio 3 and 5 also show larger peak values at distances  $z^* \simeq 0.4h$  from the corner than the cases with AR = 7 and 10. This again is explained by the fact that the secondary flow extends up to  $z^* \simeq 5h$  from the corner, and if the duct is not wide enough to accommodate the whole extent of the secondary flow, then its structure is modified by means of a different spanwise distribution of energy.

The notion that the secondary flow is stronger close to the corner and becomes gradually attenuated as the core of the duct is approached is also observed in Figure 10, where  $\langle K_y \rangle$  is shown as a function of  $z^*$  for the aspect ratio 7 and 10 cases, over the whole span  $0 \leq z^*/h \leq 10$ . Here it also becomes clear that the corner effects are relevant up to the fifth window, and beyond this point they basically become zero when long averaging times are considered. Interestingly, the side-wall boundary layer thickness  $\delta_z$  (evaluated at the plane  $y = 0$  as the point where  $dU^+/dz^+ \simeq 0$ ) rises from  $h$  to  $3h$  and to  $5h$  for the lower aspect ratios, then shows the same value  $\delta_z \simeq 6.5h$  in both AR = 7 and 10 cases. This also suggests that the corner effects start to stabilize at aspect ratio 7. It is also important to highlight that the kinetic energy of the mean flow integrated over the whole width  $\langle K \rangle_{yz}$  is roughly constant for all the aspect ratio cases and equal to  $\simeq 6.5 \times 10^{-5}$  (except for the square duct case, which has a value of  $\simeq 3 \times 10^{-5}$  as discussed above). This implies that it is possible to establish a structure for the secondary flow as a function of aspect ratio, and at least for the range of aspect ratios under consideration it is possible to evaluate the contributions from each region to the cross-flow. In order to further assess the small differences in  $\langle K_y \rangle$  between aspect ratios 7 and 10, we are currently performing a DNS on a duct with AR = 14.4. This case is also designed

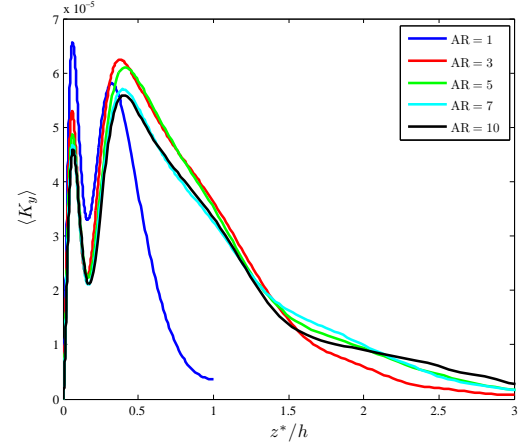


Figure 9. Spanwise variation of the wall-normal integrated kinetic energy of the secondary flow  $\langle K_y \rangle$ , for all the duct cases under consideration. Results obtained from the streamwise-averaged fields, with averaging times of at least 3,000 time units. Note that  $z^*$  is measured from the corner to allow easier comparison between the various cases.

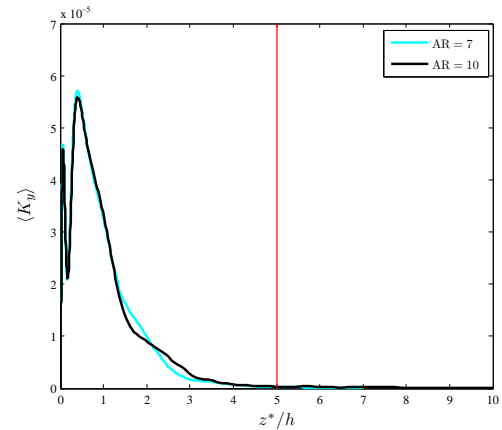


Figure 10. Spanwise variation of the wall-normal integrated kinetic energy of the secondary flow  $\langle K_y \rangle$ , for aspect ratios 7 and 10. Results obtained from the streamwise-averaged fields, with averaging times of at least 3,000 time units. Note that  $z^*$  is measured from the corner to allow easier comparison between the various cases, and the location  $z^* = 5h$  is shown to illustrate the spanwise extent of the secondary flow.

to match one of the cases in the measurements by Vinuesa *et al.* (2014a).

## SUMMARY AND CONCLUSIONS

Direct numerical simulations of turbulent duct flows with width-to-height ratios 1, 3, 5, 7 and 10, at a friction Reynolds number  $Re_{\tau,c} \simeq 180$ , were carried out with the spectral element code Nek5000. The aim of these simulations is to gain insight into the kinematics and dynamics of Prandtl's secondary flow of second kind, and its impact on the flow physics of wall-bounded turbulence. The computa-

tional setup was adequate to capture the smallest turbulent structures, as well as the complicated phenomena arising at the duct corners. Although the corners inhibit the formation of typical wall-turbulence streaks, the interaction of bursting mechanisms from horizontal and vertical walls lead to the formation of the secondary flow through redistribution of turbulent kinetic energy from the  $\bar{v}^2$  component to the  $\bar{w}^2$ .

The secondary flow in the various ducts is characterized in terms of the cross-plane mean kinetic energy  $K = (V^2 + W^2)/2$ , and its variation in the spanwise direction of the flow. Our results show that averaging times of at least 3,000 time units are required to reach a converged state of the secondary flow, which extends up to  $z^* \simeq 5h$  from the side walls. We also show that if the duct is not wide enough to accommodate the whole extent of the secondary flow, then its structure is modified by means of a different spanwise distribution of energy. Dividing the flow into windows of width  $h$  reveals a number of interesting conclusions. First, all the aspect ratios exhibit the similar levels of averaged energy close to the corner (window #1),  $\langle K \rangle_{yz1} \simeq 4.5 \times 10^{-5}$  and  $4 \times 10^{-5}$  for aspect ratios 3 and 5, and 7 and 10 respectively; the square duct shows a lower level  $\simeq 3 \times 10^{-5}$ , and its secondary flow differs from the one observed in the wider ducts. The second window shows the same level of energy in all aspect ratios from 3 to 10,  $\langle K \rangle_{yz2} \simeq 2 \times 10^{-5}$ , which is roughly ten times larger than the energy found in the fourth window for the widest cases (7 and 10). Interestingly, all the windows beyond #5 exhibit a decaying level of energy, and the rate of decay is approximately  $\langle K \rangle_{yz} \sim T_A^{-1}$ . This is the same rate of decay observed in a spanwise-periodic simulation, which suggests that beyond  $z^* \simeq 5h$ ,  $\langle K \rangle_{yz}$  behaves as a random variable with zero mean, with rate of decay consistent with central limit theorem theory. With respect to windows #4 and #5, the levels of energy from the various cases do not decay at the rate  $\langle K \rangle_{yz} \sim T_A^{-1}$ , and it is not clear whether the data would converge to a nonzero value or not. In any case, it can be stated that the flow in this region does not behave as it does in the channel. On the other hand, the dynamics of the turbulence and short-time averages of the vortical flow have revealed differences in the core region between the channel and ducts with aspect ratios up to 10 (Vinuesa *et al.*, 2015c). These non-stationary effects of the secondary flow may persist into the core for all the aspect ratios we have run so far, and may interact with the dynamics of the nominally homogeneous flow that would exist in a channel. The non-stationary effects will be presented and further discussed in the Symposium. This suggests that experimental facilities intended to represent the canonical channel flow and to compare the turbulence structures and dynamics and vortical flow details may require aspect ratios larger than facilities with highest ratios used so far of 12 and may need to be as large as 18, as in Vinuesa *et al.* (2014a). Note that these conclusions are limited to the low Reynolds number range under consideration, and additional data will be necessary to assess Reynolds number effects.

## REFERENCES

Chevalier, M., Schlatter, P., Lundbladh, A. & Henningson, D.S. 2007 A pseudospectral solver for incompressible boundary layer. Technical Report TRITA-MEK 2007:07. KTH Mechanics.

- Chong, M. S., Perry, A. E. & Cantwell, B. J. 1990 A general classification of three-dimensional flow fields. *Phys. Fluids A* **5**, 765–777.
- Fischer, P. F., Lottes, J. W. & Kerkemeier, S. G. 2008 NEK5000: Open source spectral element CFD solver. Available at: <http://nek5000.mcs.anl.gov>.
- Gavrilakis, S. 1992 Numerical simulation of low-Reynolds-number turbulent flow through a straight square duct. *J. Fluid Mech.* **244**, 101–129.
- Hunt, J. C. R., Wray, A. A. & Moin, P. 1998 Eddies, streams, and convergence zones in turbulent flows. In *Center for Turbulence Research Proceedings of Summer Program*.
- Huser, A. & Biringen, S. 1993 Direct numerical simulation of turbulent flow in a square duct. *J. Fluid Mech.* **257**, 65–95.
- Jeong, J. & Hussain, F. 1995 On the identification of a vortex. *J. Fluid Mech.* **285**, 69–94.
- Kida, S. & Miura, H. 1998 Swirl condition in low-pressure vortices. *J. Phys. Soc. Japan* **67**, 2166–2169.
- Nagib, H. M., Vinuesa, R., Prus, C. & Schlatter, P. 2014 Coherent structures in turbulent rectangular duct flows. In *67th Annual Meeting of the American Physical Society, Division of Fluid Dynamics, 24 November 2014, San Francisco, CA, USA*.
- Patera, A. T. 1984 A spectral element method for fluid dynamics: laminar flow in a channel expansion. *J. Comput. Phys.* **54**, 468–488.
- Pinelli, A., Uhlmann, M., Sekimoto, A. & Kawahara, G. 2010 Reynolds number dependence of mean flow structure in square duct turbulence. *J. Fluid Mech.* **644**, 107–122.
- Schlatter, P. & Örlü, R. 2012 Turbulent boundary layers at moderate Reynolds numbers. Inflow length and tripping effects. *J. Fluid Mech.* **710**, 5–34.
- Uhlmann, M., Pinelli, A., Kawahara, G. & Sekimoto, A. 2007 Marginally turbulent flow in a square duct. *J. Fluid Mech.* **588**, 153–162.
- Vinuesa, R., Bartrons, E., Chiu, D., Dressler, K. M., Rüedi, J.-D., Suzuki, Y. & Nagib, H. M. 2014a New insight into flow development and two dimensionality of turbulent channel flows. *Exp. Fluids* **55**, 1759.
- Vinuesa, R., Hosseini, S. M., Hanifi, A., Henningson, D. S. & Schlatter, P. 2015a Direct numerical simulation of the flow around a wing section using high-order parallel spectral methods. In *Int. Symp. Turbulence & Shear Flow Phenomena (TSFP-9), 30 June - 3 July, Melbourne, Australia*.
- Vinuesa, R., Noorani, A., Lozano-Durán, A., El Khoury, G. K., Schlatter, P., Fischer, P. F. & Nagib, H. M. 2014b Aspect ratio effects in turbulent duct flows studied through direct numerical simulation. *J. Turbul.* **15**, 677–706.
- Vinuesa, R., Schlatter, P., Malm, J., Mavriplis, C. & Henningson, D. S. 2015b Direct numerical simulation of the flow around a wall-mounted square cylinder under various inflow conditions. *J. Turbul.* **16**, 555–587.
- Vinuesa, R., Schlatter, P. & Nagib, H. M. 2015c On minimum aspect ratio for duct flow facilities and the role of side walls in generating secondary flows. *J. Turbul.* **16**, 588–606.
- Zhou, J., Adrian R. J. Balachandar S. & Kendali, T. M. 1999 Mechanisms for generating coherent packets of hairpin vortices. *J. Fluid Mech.* **387**, 353–396.